PCCP

Structural elucidation of polydopamine facilitated by ionic liquid solvation

Journal:	*Physical Chemistry Chemical Physics*
Manuscript ID	CP-ART-11-2022-005439.R1
Article Type:	Paper
Date Submitted by the Author:	08-Jan-2023
Complete List of Authors:	Singh, Abhishek; Monash University, Chemistry; IISER Kolkata, DCS Mason, Thomas; Monash University, Chemistry Lu, ZhenZhen; Monash University, Chemistry Hill, Anita; Commonwealth Scientific and Industrial Research Organisation, Materials Science and Engineering Pas, Steven; Australia Department of Defence, Maritime Division Teo, Boon; Monash University, School of Chemistry; Monash University Freeman, Benny; The University of Texas at Austin, Chemical Engineering Izgorodina, Ekaterina; Monash University, Chemistry

ARTICLE

Structural elucidation of polydopamine facilitated by ionic liquid solvation

Received 00th January 20xx,
Accepted 00th January 20xx

DOI: 10.1039/x0xx00000x

Abhishek Singh[a,b]†, Thomas G. Mason[a]†, Zhenzhen Lu[a], Anita J. Hill[c], Steven J. Pas[d], Boon Mia Teo[a], Benny D. Freeman[e] and Ekaterina I. Izgorodina[a]*

Minimal understanding of the formation mechanism and structure of polydopamine (pDA) and its natural analogues, eumelanin impedes the practical application of these versatile polymers and limits our knowledge of the origin of melanoma.[1–8] The lack of conclusive structural evidence stems from the insolubility of these materials, which has spawned significantly diverse suggestions of pDA's structure in the literature.[9,10] We discovered that pDA is soluble in certain ionic liquids. Using these ionic liquids (ILs) as solvents, we present an experimental methodology to solvate pDA, enabling us to identify pDA's chemical structure. The resolved pDA structure consists of self-assembled supramolecular aggregates that contribute to the increasing complexity of the polymer. The underlying molecular energetics of pDA solvation and a macroscopic picture of the disruption of the aggregates using IL solvents have been investigated, along with studies of the aggregation mechanism in water.

1. Introduction

Among many of nature's ubiquitous phenolics, polydopamine (pDA) has emerged as one of the most versatile materials in the last decade, with a fascinating set of interdisciplinary applications at the intersection of chemistry, physics, biology, and medicine.[11–17] Associated with the biosynthetic pathways of eumelanin, pDA has been utilized as a versatile coating material with applications spanning the fields of surface functionalization, imaging, biosensing and photothermal therapy.[1,18–24] Despite its significance in biomedical applications, the scientific community has faced challenges in the development of pDA-based chemistry due to its complex structural heterogeneity and complete insolubility in all traditional solvents, which have hindered the "complete" structural elucidation of pDA to date.[9,25–29] Solid-state techniques (such as ssNMR, FTIR, MALDI-TOF, UV-Vis and RAMAN) have given rise to two schools of thought – a self-assembled supramolecular aggregate of indoledione (IND) and dihydroxyindole (DHI) monomers (Fig. S1 B, C and H)[10,30–36] or a covalent polymer connected via aryl-aryl linkages (Fig. S1D, and J).[37,38] In both cases, the initial stage of polymerization of dopamine must go through auto-oxidation to generate cyclized dopamine-quinone structures that may polymerize further.

We envisaged ionic liquids as possible solvents to solubilize pDA due to their ability to interact through various methods including Coulombic forces given their charged nature, as well as dispersion interactions with a wide range of available chemical functionalities.[39–42] For dissolution experiments, we screened a series of ILs, consisting of 1-ethyl-3-methyl imidazolium (C_2mim^+), N-butyl-N-methyl-pyrrolidinium (C_4mpyr^+) and triethyl-butyl-ammonium (N_{2224}^+) cations (Fig. 1A). Polydopamine was prepared in basic conditions as reported in the literature (see methods) and the thus synthesized polymer aggregates were used throughout the experiment.

2. Experimental Methods

2.1 Polymer dissolution in ILs and characterisations

Polydopamine was synthesized using the method reported in the literature.[30] 100 mg of dopamine HCL was oxidized in 50 ml of 10 mmol TRIS buffer (pH = 8.5). The solution changes colour from transparent to black and polymer precipitates. After centrifugation, the precipitate was collected and dried which was found to be insoluble in all common organic solvents. This precipitate was used for further characterization. Dissolution experiments were carried out by dissolving synthesized PDA into ionic liquids without any pre-treatment. 4 mg of pDA was added to 200 μL of respective ILs in glass vials and heated without stirring on a heating plate at 100 $^\circ$C for 3 hours. Black coloured solution was then transferred to NMR tubes and solubility was confirmed by ^{1}H-NMR. Nuclear magnetic resonance spectra were collected using a Bruker DRX-400 and

[a] School of Chemistry, Monash University, Clayton, Melbourne, VIC 3800, Australia. E-mail: katya.pas@monash.edu
[b] IITB-Monash Research Academy, Bombay 400076, India
[c] Manufacturing, CSIRO, Clayton, VIC 3168, Australia
[d] Maritime Division, Defence Science and Technology Group, Department of Defence, 506 Lorimer St Fisherman's Bend, VIC 3207, Australia
[e] Department of Chemical Engineering, The University of Texas at Austin, Austin, TX 78712, USA
† Contributed equally

Electronic Supplementary Information (ESI) available. [A repository containing all required simulation files, OpenMM scripts and details of the aggregation analysis can be found at https://github.com/tommason14/dopamine-MD]. See DOI: 10.1039/x0xx00000x

Bruker DRX-600 with signals reported in ppm and referenced against TMS. POM images were captured at 0, 1, 2, 4, 10, 20 and 60, 90 and 130, 160, 210 mins after dissolving PDA in respective ILs and heating at 100 °C. POM photomicrographs were obtained using a CCD camera (Flea3, Point Grey, Richmond, BC, Canada) coupled to a polarizing light microscope (Kozo XJP 300). All images were collected after the sample was cooled to room temperature followed by sonication for 2 mins. To detect the approximate solubility limit 1 mg of pDA was dissolved in 200 μL of ionic liquid, the sample was heated, and POM images were collected at regular intervals as mentioned above. Once we could not see any particles with POM, 1 mg pDA was further added to the same sample vial and the process was repeated until the disappearance of particles ceases after heating for at least 120 minutes.

To investigate any change in the chemical nature of the pDA which might occur during the dissolution, polymer was brought back in the dry state by reprecipitating dissolved pDA from the ILs using preferential solubility of ILs in ethanol and acetone. For this purpose, ethanol was added to the 200 µL of dissolved solution of pDA in IL to make up to solution to the 30 mL and the resulting mixture was stirred vigorously in a closed container and centrifuged at 7500 amp. The transparent liquid was decanted from the mixture and filled again with ethanol up to 30 mL. The same procedure was repeated about 10 times till the polymer settled down in powder form (10 X 30 mL). After this, the powdered was washed with acetone and centrifuged using the above-mentioned procedures (2 X 30 mL) and dried in a vacuum oven at 50 °C for 12 hours to obtain the final product. This powder was used for powder X-ray diffraction, TEM, and FTIR characterisations. Powder x-ray diffraction (XRD) measurements were performed using a Bruker D8 ADVANCE Eco powder x-ray diffractometer (Bragg–Brentano θ–θ geometry) with CuK_α radiation (λ = 1.5406 Å) at room temperature and processed using the Bruker DIFFRAC SUITE software. The Fourier Transform Infrared (FTIR) spectrum was obtained using a Cary 630 FTIR Spectrometer. The morphology of pDA was measured by transmission electron microscopy (TEM). Images were obtained using a FEI Tecnai G2 T20 electron microscope, operated at 200 kV, using LaB_6 emitter.

2.2 Aggregation mechanism via molecular dynamics simulations:

Polarisable molecular dynamics was undertaken using the modified forms of the OPLS-AA forcefield.[43]Water was described using the SWM4-NDP model proposed by Lamoureux et al.[43] [C_2mim][OAc] was described by the CL&Pol[44] forcefield while OPLS-AA parameters were found using Ligpargen[45] for each solute molecule. Atomic partial charges for each solute were calculated using SRS-MP2/cc-pVDZ geometries at the M062X/cc-pVTZ level using the CHELPG partitioning scheme in Gaussian16.[46] Atomic polarizabilities for all solute molecules were calculated via M062X/cc-pVTZ calculations in an applied electric field of 0.0008 au, with molecular properties decomposed into atomic contributions via Stone's GDMA software and analysis scripts published by Heid et al.[47,48] The same procedure was used when parameterizing the CLPol forcefield, which contains the atomic polarizabilities for [C_2mim][OAc].[49] Note that while the original publication by Padua and Goloviznina used the truncated SadleJ basis set, higher order basis functions were required for the calculations of the dimers to converge, therefore cc-pVTZ was used as an alternative.

All non-hydrogen atoms are considered polarizable, with polarizabilities of hydrogens summed onto the attached heavy atoms. Each Drude particle has a mass of 0.4 g mol^{-1} and is attached to the Drude core via a harmonic bond with a force constant of 4184 kJ mol^{-1}. Partial charges of each Drude particle are determined from the atomic polarizabilities, as $\boldsymbol{\alpha = q_D^2/k_D}$.[50] All hydrogens are considered identical with α = 0.323 Å^3. Polarizabilities for [C_2mim][OAc] were taken from the CLPol forcefield, while values for each heavy atom in each solute were calculated here. Values are found in tables S1-4.

The addition of Drude particles requires scaling of Lennard-Jones terms to avoid overestimating polarization effects, with these scaling factors termed k_{ij} values by Padua *et al*.[51] SAPT0/aug-cc-pVDZ calculations were performed over a range of separations for all solute-IL, IL-IL, solute-solute and solute-water interactions. The configuration with the greatest total interaction energy was taken and intermolecular interactions were calculated at the SAPT2+/aug-cc-pVDZ level, with k_{ij} values calculated as a ratio of dispersion to induction:

$$k_{ij} = \frac{E_{disp}}{E_{disp} + E_{ind}}$$

Water-water interactions were not scaled as these are adequately described by the standalone SWM4-NDP forcefield. Lennard-Jones radii (σ) of simulations with [C_2mim][OAc] were scaled by 0.985 as this is shown to improve density predictions.[49] Simulations involving water had σ values scaled by 0.975. Required values for LJ scaling are shown in tables S5 and S6.

The indoledione terms were also used for every other solute molecule – SAPT2+/aug-cc-pVDZ calculations of the DHI-indoledione dimers are computationally unfeasible. Short range dipole-dipole interactions involving the Drude particles were reduced using Thole damping with α = 2.6, whilst polarization catastrophes were avoided by applying Tang-Toennies damping to the interactions involving the hydroxyl atoms and the Drude particles, with b = 4.5 and c = 1.[52,53] All simulations were performed using OpenMM.[54] Use of the temperature-grouped Nosé-Hoover thermostat properly maintains the temperature of atoms and Drude particles.[55] The temperature of Drude cores was set to 300 K while Drude particles were thermalized to 1 K throughout the entire study. Pressure applied during equilibration was implemented through a Monte-Carlo barostat. A timestep of 1 fs was used and the particle-mesh-Ewald scheme was used to handle long-range electrostatics, with vdW and electrostatic interactions cut off at 12 Å. All bonds involving hydrogen atoms are constrained with the SHAKE algorithm. Velocities were modulated every 10 steps to prevent the center of mass of the simulation box from drifting. In each simulation, 20 π-systems were present along with 2000 water molecules or 500 IPs [C_2mim][OAc] in a ~ 50 Å box. This means each simulation box contained either 20 monomers, 10 dimers or 10 monomers mixed with 5 dimers. All simulations were equilibrated for 5 ns in the NpT ensemble at 300 K and 1 bar, and production simulations were ran at 300 K for 150 ns in water, and

200 ns in [C_2mim][OAc]. Aggregation analysis was performed using the Gromacs *gmx clustsize* program with a 4 Å cut-off, using the entirety of each production simulation. Correlations between intermolecular distances and angles between the $\boldsymbol{\pi}$-systems of each solute molecule were calculated using TRAVIS.[56]

For example, consider the DHI simulations, structure A, in water. The average number of DHI molecules in the largest cluster was calculated as 11.6 when using a cut-off of 4 Å to determine which cluster each molecule resides in and then averaging across all frames of the trajectory. The cluster size was then given as a proportion of the 20 solute molecules in the simulation, for example 11.6/20 x 100 % = 58.2 %. In the case of the two dimers, structures C and D, only 10 solute molecules were present. The average number of molecules in the largest cluster in water was 8.2, or 8.2/10 x 100 % = 82 %.

2.3 Energetics of solvation via ab-initio calculations

Computational investigations were undertaken using GAMESS-US[57] for geometry optimizations and single point energy calculations, at the FMO2-SRS-MP2/cc-pVDZ and FMO3-SRS-MP2/cc-pVTZ levels of theory respectively.[58–61] The Fragment Molecular Orbital (FMO) theory has been discussed at length previously - here we will mention that FMO improves computational efficiency by parallelizing any computation over a number of physical nodes, enabling near linear scaling - a clear advantage over the O(N^5) scaling of conventional second-order Møller-Plesset perturbation theory.[62] Meanwhile, spin-ratio-scaled MP2, a method developed in our group, achieves CCSD(T) accuracy with the expense of a conventional MP2 calculation, saving computational resources.[63] After optimization with SRS-MP2, GAUSSIAN16 was used to investigate fluorescence of systems likely to facilitate photoexcitation, using time-dependent DFT at the $\boldsymbol{\omega}$B97XD/aug-cc-pVDZ level of theory. Thermal relaxation of excited states was achieved with excited state optimizations.

Intermolecular interaction energies were calculated using either GAMESS or Psi4[64] at the SRS-MP2/cc-pVTZ level.[65] Boltzmann weighted intermolecular energy (E_{INT}) was defined as follows:

$$E_{INT(ave)} = \frac{\sum_{i=1}^{N} E_{INT,i} \cdot e^{-\frac{E_{INT,i}}{RT}}}{\sum_{i=1}^{N} e^{-\frac{E_{INT,i}}{RT}}}$$

Where *N* is the number of energetically preferred configurations considered (usually 3) and *i* refers to the individual configuration.

The algorithmic differences of each software are cancelled out when finding energetic differences, therefore comparisons can be made between interaction energies calculated with either package. Molecular orbitals were obtained via GAUSSIAN16 using HF/cc-pVTZ, while atomic charges were computed using the surface-based Geodesic charge scheme available in GAMESS using the same computational method and basis set.[66] It must be noted that gas-phase geometry optimisations underestimate intermolecular distances in ionic liquid ions[67] and therefore, the presented results on intermolecular energy should be considered the upper bound to those accounting for solvation energy of ionic liquids.

2.4 Transition state calculations

Transition states were calculated at the $\boldsymbol{\omega}$B97xD/aug-cc-pVTZ level of theory with solvent corrections approximated using M05-2X/6-311+G**. The SMD solvation model was implemented here, the rationale being that M05-2X was used when parameterizing the SMD solvation model.[68] Water was used as the solvent to mimic the conditions of polymerization.

Enthalpies (H) and entropies (S) were calculated using molecular partition functions,[69] using the eigenvalues of the Hessian matrix generated from a Gaussian16 frequency calculation calculated at the same level of theory as the optimization, M06-2X/cc-pVDZ with SMD solvation ($\boldsymbol{\epsilon}$= 80.4). Single point energy calculations provide the electronic energy of the system (E_0), while the zero-point vibrational energy (ZPVE) must be added to increase the energy of that electronic minima to accurately represent the system at 0 K. Solubility studies were performed at 100 °C, and therefore temperature corrections were applied to the enthalpic terms to mimic experimental conditions.

Note that the temperature correction is necessary to provide corrections for additional translations, vibrations and rotations that occur at elevated temperatures for a given vibrational frequency, $\boldsymbol{\nu_i}$:[70]

$$TC = R\sum_i \frac{h\nu_i/k_B}{exp(h\nu_i/k_BT) - 1} + \frac{5}{2}RT + \frac{3}{2}RT$$

Transition state enthalpies were calculated using the following equation:

$$\boldsymbol{\Delta H^{\ddagger} = (E_0 + ZPVE + TC)_{TS} - (E_0 + ZPVE + TC)_{reactants}}$$

Entropic contributions are calculated using total entropy, given as a sum of electronic, vibrational, rotational and translational terms, with low energy vibrations treated using the hindered internal rotor:

$$\boldsymbol{\Delta S^{\ddagger} = S_{TS}^{Total} - S_{reactants}^{Total}}$$

with Gibbs free energies calculated as follows:

$$\boldsymbol{\Delta G_{solv}^{\ddagger} = \Delta G_{gas}^{\ddagger} + \Delta\Delta G_{solv}}$$

where

$\boldsymbol{\Delta G_{gas}^{\ddagger} = \Delta H^{\ddagger}}$(**ω**B97xD/aug - cc - pVTZ, gas) $-$ $\boldsymbol{T\Delta S^{\ddagger}}$(**ω**B97xD/aug - cc - pVTZ,

and

$\boldsymbol{\Delta\Delta G_{solv}} = \boldsymbol{\Delta G_{solv}}$(M05 - 2X/6 - 311 + G**) $-$ $\boldsymbol{\Delta G_{gas}}$(M05 - 2X/6 - 311 + G**)

For the anti-dimer, an energy barrier of 115 kJ mol^{-1} was obtained between the reactants and dimeric transition state, indicating that dimerization is plausible. To find the transition state of the reaction to form the syn-dimer, the central C-C bond of the dimer was elongated as though a radical addition was occurring. As such, energies of the monomers were calculated with doublet multiplicity. "Conventional" starting configurations resulted in both 2-2 and 2-3 bonds forming in the transition state, whereas a stacking arrangement (in an "early" transition state) resulted in only the desired 2-2 bond forming. Subsequently, there is a large reduction in energy associated with the progression from the transition state to the product as a significant rearrangement is necessary. Regardless, a transition state barrier of 37.1 kJ mol^{-1} also shows that syn-dimer formation is plausible. Raw data for both transition states are shown in tables S9 and S10.

2.5 Experimental and Computational Fluorescence measurements

Experimental spectra were recorded over the course of a polymerization in water, and simulated spectra of monomeric, dimeric, and tetrameric aggregates were compared to these results.

To investigate fluorescence of dopamine aggregates in water, SRS-MP2 optimized geometries were used. Theoretical spectra were calculated with time-dependent DFT using GAUSSIAN16 at the ωB97XD/aug-cc-pVDZ level. SMD solvation was applied to all TD-DFT calculations, using water as the solvent to replicate experimental

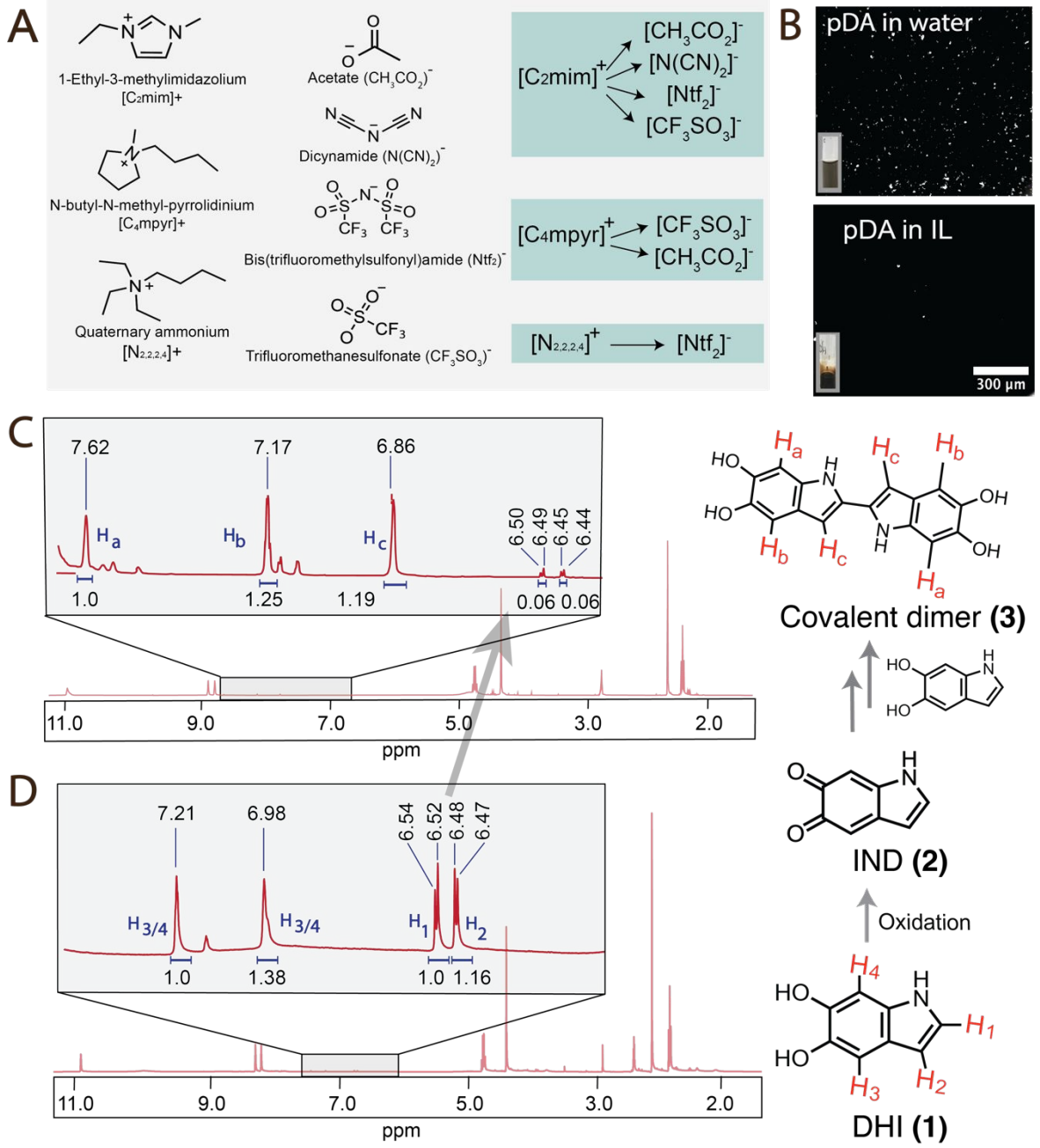

Fig. 1. Structural analysis of pDA solvated in NMR. (A) Three sets of ILs used in the study **(B)** POM images of 2 mg of pDA dispersed in 2 mL of water and 5 mg of pDA in 400 µL of $[C_2mim][OAc]$ (scale bars for both images are 300 ⍰M), **(C)** ^{1}H-NMR for dissolved pDA in $[C_2mim][OAc]$ using DMSO-d_6 as deuterated solvent, and **(D)** ^{1}H-NMR for dissolved pDA in $[C_2mim][OAc]$ using acetone-d_6 as deuterated solvent and proposed reaction scheme for pDA. Cyclised dopamine (DHI) 1, Indolequinone (IND) 2 and covalent dimer, 3 as identified from ^{1}H-NMR.

polymerization conditions. Many configurations are found to absorb at wavelengths similar to experimental values, with the inclusion of a hydroxyl group, or a mixture of the either carbonyl or hydroxyls groups appearing to absorb in the region found experimentally. One important conclusion from fig. S16 is that the presence of a carbonyl peak on both monomers of the dimeric aggregate leads to no absorption – a mixture is required, facilitating the dimerization shown below.

A promising result is that simulating stacking of monomers recovers enough of the non-covalent intermolecular dispersion interactions present in the bulk to accurately predict absorption wavelengths, with good agreement to experiment found with many of the configurations tested. Note that absorption here is assumed to occur

with no change in the geometry as excitation from the ground state is performed, obeying the Franck-Condon principle. As such, absorption here represents a transition to a higher lying vibrational level of the first excited state: S1(v = n) ← S0(v = 0). To predict fluorescence, we must induce thermal relaxation, allowing for a change in geometry as the molecule transitions to the lowest lying vibrational level of the first excited electronic state: S1(v = n) → S1(v = 0). This result is achieved by performing optimizations of the geometry in the excited state, specifying an electronic level at which the ground is excited to, found from the intensity of transitions found from the calculations used to predict ground state absorption. The emission spectra obtained at the final step of the excited state optimization is assumed to be fluorescence that is observed experimentally, assuming that the optimized geometry of the excited state refers to the molecule in the S1(v = 0) vibronic state. The fluorescence reported in fig. S17 therefore refers to the transition down to a high lying vibrational level of the ground electronic state: S1(v = 0) → S0(v = n).

Fig. S16 shows that the presence of a C=C bond between the C2-C3 carbons of indole, along with carbonyl groups attached to the C5 and C6 carbons of indole (variant 4 of fig. S14) may be responsible for the fluorescence observed experimentally. Likewise, having a dimeric aggregate of either variants 1 and 4 or 2 and 3, varying both the carbonyl/hydroxyl groups as well as a double or single bond between the C2-C3 carbons, results in fluorescence wavelengths that are comparable to experiment. To summarize fig. S17 briefly, fluorescence observed experimentally arises from transitions of multiple dopamine variants - one variant alone is not responsible for the spectra observed experimentally. Absorption of tetramer aggregates of cyclized dopamine were also calculated and shown in fig. S14, using aggregates of variant 4 in fig. S15. There is a red shift present here, with a large absorption at 220 nm shown for the monomer, transitioning to 320 nm for the stacked dimer. An important note is that when absorption of tetramer aggregates is calculated, there is no absorption present below 500 nm. Experimental wavelengths above 400 nm were not scanned, and so fluorescence of tetramer aggregates could not be measured experimentally, validating the experimental hypothesis that monomer aggregation leads to reduced fluorescence, at least in the wavelength range measured experimentally.

3. Results and Discussions

3.1 Solubility and ^{1}H-NMR characterization of pDA

[C_2mim][OAc] was the only IL we found that dissolved pDA without any pre-treatment of the material, as confirmed by polarized optical microscopy (POM) and ^{1}H-NMR spectroscopy (Fig. 1B, C and D and Fig. S4)POM of much higher concentration of pDA in ILs (5 mg of pDA in 400 µL) yielded images that showed a negligible number of pDA particles when compared to the images of pDA in water at low concentrations (2 mg of pDA in 2 mL, Fig. 1B).

Highly viscous [C_2mim][OAc], significantly suppresses the intensity of the solute peaks (see ^{1}H-NMR spectra of pure [C_2mim][OAc] (Fig. S2) and dopamine hydrochloride dissolved in [C_2mim][OAc] (fig. S3)). All NMR spectra were measured by transferring a part of the stock solution to deuterated acetone or deuterated DMSO. ^{1}H-NMR spectra recorded with acetone-d_6 (Fig. 1D) clearly show evidence of an indole-like cyclized dopamine structure **1** (Fig. 1), supporting previous hypotheses.[30] Two possible structures were found based on coupling patterns and integrals: 5,6-dihydroxyindole (structure **1** in Fig. 1) and its oxidized form indole-5,6-dione (structure **2** in Fig. 1). The absence of protons in the aromatic and aliphatic regions suggested that the liquid predominantly contains cyclized monomeric units of dopamine. These findings suggest that pDA consists of cyclized dopamine units, ruling out the possibility of uncyclized covalent trimeric structures as reported previously,[36] in which case aliphatic proton shifts in ^{1}H-NMR would be present as the major constituent.

We further investigated the ^{1}H-NMR spectra of a pDA-[C_2mim][OAc] suspension dissolved in DMSO-d_6 (Fig. 1C), since DMSO can act as a co-solvent with ILs to aid cellulose dissolution.[71,72] Interestingly, we found features of not only cyclized monomeric units, but also covalent dimeric units bonded through the C2 carbon of the indole-like unit (structure **3** in Fig. 1). The spectra recorded in DMSO-d_6 also contain monomeric peaks, but these peaks were significantly less intense as compared to those responsible for the dimeric unit. These results lead us to conclude that the monomeric form of DHI (**1**) and IND (**2**) are minor products, whereas the major product in the polymerization comes in the form of a covalent dimer (**3**). We also tested acetonitrile-d_3, benzene-d_6, methanol-d_4 and deuterated chloroform. However, these co-solvents did not aid solubility. To ensure that pDA did not undergo any chemical modification due to interactions with the IL, pDA was regenerated from the IL solution by adding water to induce phase separation, precipitating as a black powder in the aqueous phase. The centrifuged material was characterized by transmission electron microscopy (fig. S5) and infrared spectroscopy (fig. S6), and these results were identical to those of the pDA originally polymerized in aqueous solution.

3.2 Polarizable molecular dynamics simulations to probe the aggregation propensity

Given the experimental findings, we now aim to study the process of how these cyclized monomeric units and covalently linked dimers give rise to the final polymeric structure. To do this, polarizable molecular dynamics simulations were used to probe the likelihood of aggregation of molecules 1, 2 and 3,

ARTICLE

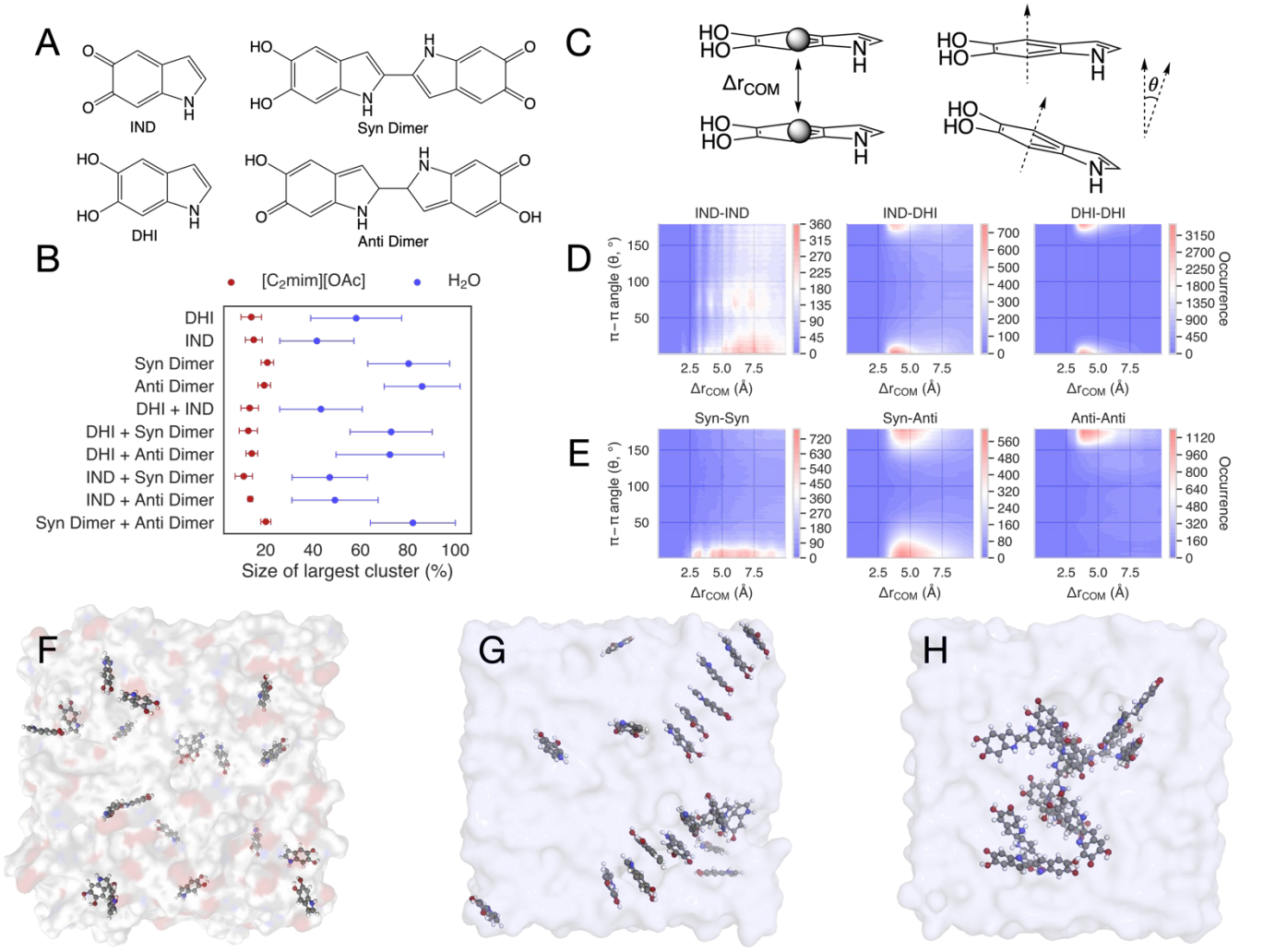

Fig. 2. Polarizable molecular dynamics simulations to probe the aggregation propensity. A) Monomeric and dimeric dopamine species used in MD simulations to study supramolecular aggregation. B**)** Average number of molecules in the largest aggregate, shown as a percentage of the number of species per simulation. Error bars show standard deviations. **C**) Criterion used to quantify aggregation – measuring the distances between the center of masses (Δr_{COM} in Å) and angles (θ, in degrees) of planes bisecting each pair of π-conjugated solute molecules. **D,E)** Correlation as described in **C** between IND and DHI in **(D)** and the syn-dimer and anti-dimer in **(E)** in water. Angles of 0 or 180° demonstrate perfect alignment of the two molecules. Red regions indicate areas where neighboring molecules occur most often across the simulation, while the blue regions show distances and angles that are rarely observed. **F,G,H)** Typical snapshots of solute molecules from simulations showing 20 monomers of DHI in [C_2mim][OAc] **(F)**, 20 monomers of DHI in water **(G)** and 10 dimers of the anti-dimer in water **(H)**.

identified via the NMR experiments. Simulations of one solute contained 20 molecules of structures A or B, or 10 molecules of structures C or D, as shown in Fig. 2A. Meanwhile simulations of multiple solutes contained 10 species of A or B and five species of dimers C or D, or in the case of two dimers, five species of C and 5 species of D. Thus, the number of functional groups that facilitate π-stacking remained constant across all simulations. Each solute was then solvated by either 2000 water molecules (production runs of 200 ns) or 500 ion pairs of [C_2mim][OAc] (production runs of 200 ns) in a ~ 50 Å cubic box (for more detail see methods). Raw data produced by *gmx clustsize* on the size and longevity of formed aggregates are shown in fig. S10. In the case of water simulations the aggregates formed in the beginning remained intact throughout the simulation, whereas in the case of [C_2mim][OAc], the formation of aggregates was momentous.

The size of aggregates scales linearly with the percentage of aggregated species in the largest cluster. The latter was

calculated as a percentage with respect the number of monomer/dimer molecules of dopamine included in the simulation (for more detail see the supplementary materials). Fig. 2B shows the percentage of aggregated species in the largest cluster averaged across all trajectory frames, highlighting the ability of [C_2mim][OAc] to successfully perturb aggregation and favour the formation of smaller aggregates (15.3 % of clusters in each simulation on average), leading to more effective dissolution. In contrast, dopamine species aggregate much more effectively in water via intermolecular π stacking interactions, with an average aggregate size of 63 %. Crucially, covalent dimers tend to aggregate more readily than monomers, agreeing with ^{1}H-NMR spectra that show oligomerization occurs prior to aggregation. Regarding the presence of unreacted monomers in the final product, DHI aggregates with covalent dimers 20-30% more effectively than IND.

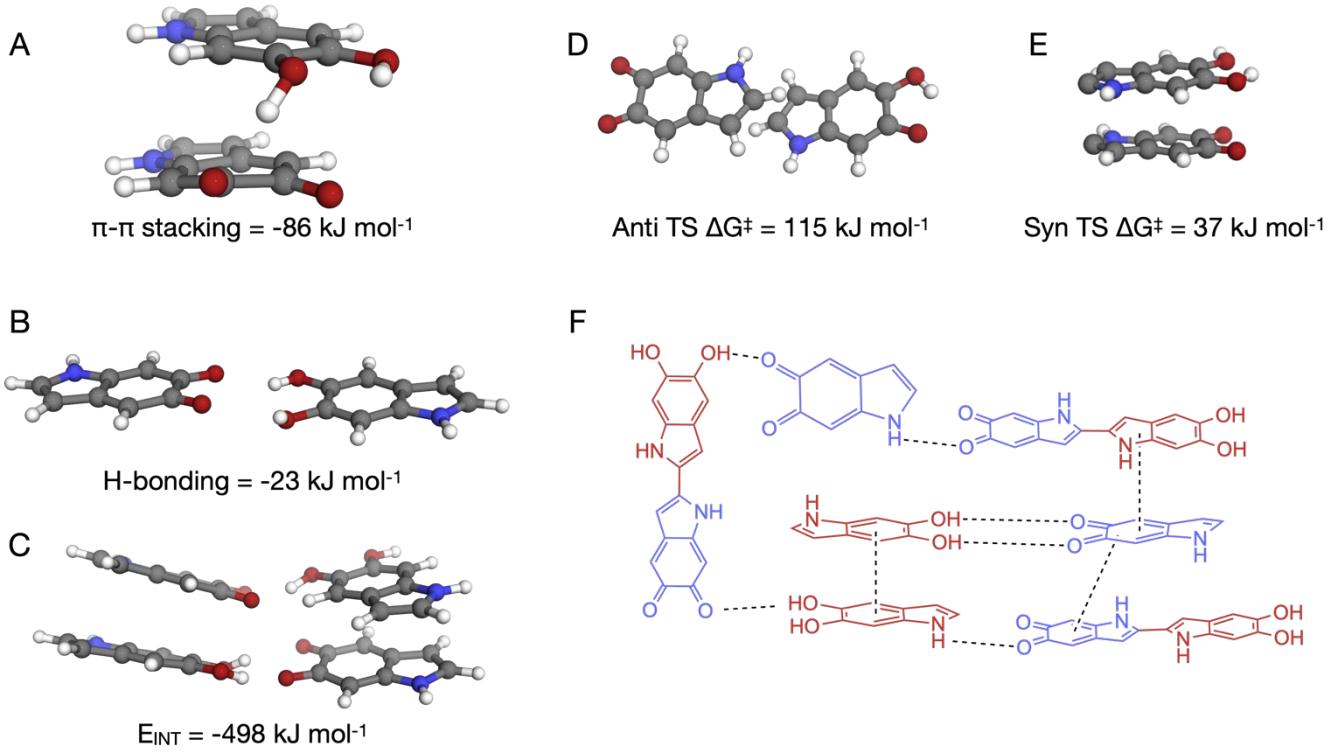

Fig. 3. Deciphering the aggregation energetics via *ab initio* calculations. (**A**) An example of strong π-π interactions between dopamine monomers, (**B**) An example of in-plane hydrogen bonding interactions. (**C**) An example of a supramolecular aggregate consisting of two IND and two IND units exhibiting strong intermolecular interactions, and (**D, E**) Transition state structures of the Anti (**D**) and Syn (**E**) dimers. (**F**) Schematic showing the proposed supramolecular structure of pDA comprised of monomeric and dimeric units linked by π-π stacking and hydrogen bonding interactions.

Fig. 2C, D and E show the correlation between intermolecular distances and angles between neighbouring π-conjugated moieties to quantify the supramolecular aggregation of dopamine species. Regions of chemical space sampled often throughout a simulation are coloured red. Ab initio calculations performed on a pair of stacked IND monomers show that optimal π- π stacking occurs at a separation of 3 to 4 Å (fig. S9), while the angle between the π-conjugated moieties should be close to 0 or 180° , resulting in the optimal π-orbital overlap.

A mixture of *syn* and *anti*-dimers shows that *anti*-dimer aggregation is plausible, with intermolecular separation ranging from 3 to 5 Å, in agreement with the *ab initio* calculations mentioned above. Meanwhile, *syn*-dimer intermolecular distances lie outside the cut-off for supramolecular aggregation, with intermolecular distances in excess of 7 Å, so there is a preference for *anti*-dimer formation. In the mixture of DHI and IND, aggregates including DHI fit the criterion for supramolecular aggregation, whereas aggregates containing only IND interact to a lesser extent with larger intermolecular distances ranging from 5 to 7 Å, and with a larger distribution of angles that prevent significant aggregation. Supporting this view, DHI aggregation is also 10-fold more prevalent than IND aggregation. This analysis suggests that the final polymer primarily includes DHI and *anti*-dimer species, with a smaller proportion of IND and *syn*-dimers present. Given that the initial dopamine cyclization produces IND molecules, the concentration of IND is likely reduced over time due to formation of covalent dimers. Snapshots of simulations of DHI in [C_2mim][OAc] and water, along with the *anti*-dimer in water, are shown in Fig. 2F, G and H to highlight the influence of changes in both solute and solvent on aggregation behaviour.

3.3 Deciphering the aggregation energetics via *ab initio* calculations

To decipher the remarkable aggregation tendency of DHI, IND and their covalent dimers seen in polarizable MD simulations, we computed aggregate energetics via *ab initio* calculations

(see methods). All possible combinations of oxidized (*e.g.,* IND) and reduced (*e.g.,* DHI) species of the cyclized dopamine monomeric units were tested (fig. S14). The highly conjugated nature of these monomers combined with either carbonyl and hydroxyl groups led to the formation of π stacked and hydrogen-bonded pairs, with the π stacked pair between IND and DHI producing the strongest interaction energy of -86 kJ mol^{-1} (Fig. 3A, table S8). π stacking was energetically preferred over hydrogen bonding, with the latter giving an interaction of -23 kJ mol^{-1} (Fig. 3B). These findings support previous evidence outlining the possibility of supramolecular polymerization.[35] An example of the associative structure formation is demonstrated in Fig. 3C. Consisting of two DHI and two IND units, the structure was found to have a very strong interaction of -498 kJ mol^{-1} (-124 kJ mol^{-1} per monomer), further confirming the energetic drive to form an associative polymer. Furthermore, the Gibbs free energy barrier of dopamine *anti*-dimerization was found to be 115 kJ mol^{-1} with dimeric product stabilization of 107 kJ mol^{-1} relative to the transition state (Fig. 3D, fig. S19-S22, and methods), while *syn*-dimerization produced a barrier of 37 kJ mol^{-1} (Fig. 3E). These findings indicate that the formation of *anti* and *syn* dimers is energetically possible, supporting the experimental evidence for the existence of covalent dimers in pDA and prompting us to propose the supramolecular structure of pDA consisting of aggregation of monomers and covalent dimers of cyclized dopamine, held together via strong π stacking and in-plane hydrogen bonding (Fig. 3F).

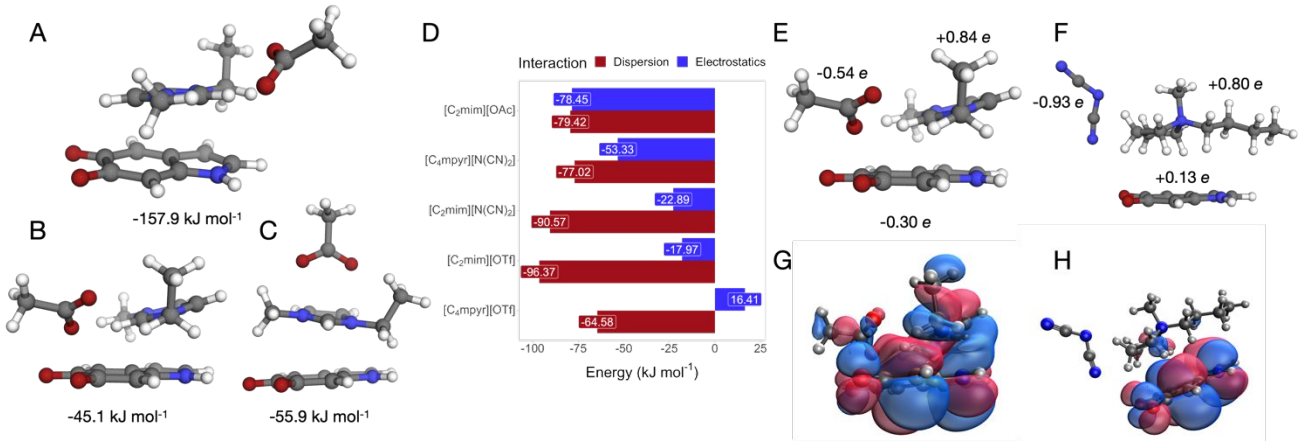

Fig. 4. Solvation energetics in ILs. (**A,B,C**) Three energetically preferable configurations of IND interaction with a single ion pair of [C_2mim][OAc], (**D**) Boltzmann-weighted interaction energies together with electrostatic and dispersion components of the IND···IL complexes for [C_2mim][OAc], [C_2mim][N(CN)$_2$], [C_2mim][OTf], [C_4mpyr][N(CN)$_2$] and [C_4mpyr][OTf], (**E,F**) Total charges of IND and the cation and anion in the single ion pair of **E**) [C_2mim][OAc] and **F**) [C_4mpyr][N(CN)$_2$], (**G**) HOMO of the most energetically stable IND···[C_2mim][OAc] complex showing contributions from all species and (**H**) HOMO of the most energetically stable IND···[C_4mpyr][N(CN)$_2$] complex showing a negligible contribution from the IL ion pair.

Experimental absorption spectra were recorded in TRIS buffer throughout the polymerization, with the observations that intensity decreased over time (fig. S14). To study which molecules are present at start of the polymerization, we simulated absorption spectra of stacked DHI and IND molecules along with their saturated forms (fig. S15). Structures containing hydroxyl groups absorb in the same regions as the experimental absorption and, therefore, DHI may be always present during the polymerization, among other species (fig. S16). Predicted fluorescence of stacked monomers show that a mixture of oxidation states and C=C saturation emit in the desired region, further supporting our hypothesis (fig. S17). Simulated fluorescence spectra of larger aggregates also show that pDA forms a supramolecular structure as dimeric and tetrameric aggregates displayed a significantly reduced level of absorption as compared to the stacked monomers, consistent with the experimental observations (fig. S18).

3.4 Solvation energetics in ILs

Solvation of pDA requires a solvent system with the ability to overcome the favourable aggregation demonstrated by DHI, IND and their covalent dimers. ^{1}H-NMR spectra (fig. S7) of pDA solvated in [C_2mim][OAc] show significant upfield shifts in signals attributed to the acidic proton of the imidazolium cation at the C2 position, highlighting strong solute-solvent interactions, which is also observed in other applications of imidazolium-based ILs.[73,74] These interactions were studied using *ab initio* calculations by arranging a single ion pair of the IL around IND, with three energetically preferred configurations shown in Fig. 4A-C. These configurations were chosen based on the preliminary assessment that the π stacking interaction between the indole ring and the imidazolium/pyrrolidinium ring produced stronger interaction energies. The position of the anion was chosen based on the previously reported studies showcasing energetically preferred positions of ionic liquid anions around imidazolium/pyrrolidinium cations.[75,76] In addition to [C_2mim][OAc], interactions of IND with [C_2mim][N(CN)$_2$], [C_2mim][OTf], [C_4mpyr][N(CN)$_2$] and [C_4mpyr][OTf] were also studied since these were unsuccessful in dissolving pDA. Out of the three configurations studied, the configuration shown in Fig. 4A, in which the anion did not directly interact with IND, was the most thermodynamically stable due to attractive electrostatic forces. However, electrostatic interactions were repulsive in the other

configurations (Fig. 4B and 4C). Only when the anion interacted with the cation through the C2-H bond of the imidazolium ring were the electrostatic effects favourable.

[C_2mim][OAc] displayed the largest overall Boltzmann-weighted interaction energy of -158 kJ mol^{-1} with IND (Fig. 4D), while the other ILs produced weaker interactions by 30 to 40 kJ mol^{-1}. These results highlight the ability of [C_2mim][OAc] to disrupt intermolecular interactions between cyclized dopamine monomers and their covalent dimers. Decomposition of interaction energies into electrostatic and dispersive components showed that dispersion interactions were significant in all ILs studied, ranging between -65 and -96 kJ mol^{-1}. The difference arises from the fact that electrostatic interactions were 25 to 60 kJ mol^{-1} less negative in all ILs when compared to [C_2mim][OAc], with [C_4mpyr][OTf] displaying repulsive electrostatics of +16 kJ mol^{-1}. ILs showing a reduced electrostatic contribution were unsuccessful in dissolving pDA, demonstrating that attractive electrostatic interactions are crucial in determining whether a solvent will dissolve pDA. We further note that the resulting dual (electrostatic/ionic and dispersive/organic) nature of [C_2mim][OAc] it more likely to control solubility[77] and catalytic properties[78,79] for preparation of biomaterials.

Polydopamine dissolution in [C_2mim][OAc] is accompanied by a net charge transfer effect from the IL ions to the π-conjugated moiety of the cyclized dopamine. The acetate anion donates as much as 46% of its electron density to the neighbouring cation, while any electron density not accepted by the cation is donated back to the dopamine monomer, producing a total charge of 0.30 e on IND (Fig. 4E). In contrast, using [C_4mpyr][$N(CN)_2$] causes IND to partially donate its electron density to the cation, with IND becoming slightly positive with a total charge of +0.13 e (Fig. 4F), thereby reducing the electrostatic interaction in the complex. This observation is not surprising since, compared to pyrrolidinium ILs, imidazolium ILs encourage a larger net charge transfer between the cation and anion regardless of the interaction site on the former. The possibility of charge transfer with the [C_2mim][OAc] ion pair was also observed in the HOMO of the IND…IL complex (Fig. 4G). Significant orbital overlap between the imidazolium cation and IND was observed which facilitates the charge transfer process. Contrasting findings were observed for the other ILs, with the cation and anion contributing negligibly to the HOMO of IND as shown in the case of [C_4mpyr][$N(CN)_2$] in Fig. 4H (HOMO visualizations of all other complexes are given in fig. S24). In summary, these results highlight the ability of [C_2mim][OAc] to donate charge to facilitate the dissolution of pDA.

Conclusions

The presented results confirm that dopamine polymerization in basic conditions results in supramolecular aggregation of monomeric and covalent dimeric structures with mixed oxidation states, containing both hydroxy indoles and quinone moieties. The procedures outlined here utilizing ionic liquids can be used to overcome solubility issues in the characterization of important biopolymers such as melanin. Understanding structure/property relationships of such materials will lead to a myriad of new possibilities for not only mimicking the fascinating functions of these biopolymers for surface functionalization and bio-sensing but also understanding diseases such as melanoma.

Author Contributions

Conceptualization: EII, SJP, BDF, AJH
Methodology: EII, AS, TGM, ZL, BMT, SJP
Investigation: AS, TGM, ZL, EII
Visualization: AS, TGM
Project administration: EII
Supervision: EII, BMT, BDF
Writing – original draft: AS, TGM
Writing – review & editing: AS, TGM, ZL, AJH, SJP, BMT, BDF, EII

Conflicts of interest

There are no conflicts to declare.

Acknowledgements

EII and BDF acknowledge a generous allocation of computational resources from the Monash *e*Research centre, the National Computational Infrastructure, and the Texas Advanced Computing Center. This work was supported by the IITB-Monash Research Academy through a PhD scholarship for AS and the Australian Research Council through a Research Training Program scholarship for TGM.

Reference

1 Y. Liu, K. Ai and L. Lu, *Chem Rev*, 2014, **114**, 5057–5115.

2 J. D. P. N. D. Simon, *Acc Chem Res*, 2010, **43**, 1452–1460.

3 S. Ito, *Pigment Cell Res*, 2003, **16**, 230–236.

4 M. d'Ischia, K. Wakamatsu, F. Cicoira, E. Di Mauro, J. C. Garcia-Borron, S. Commo, I. Galván, G. Ghanem, K. Kenzo, P. Meredith, A. Pezzella, C. Santato, T. Sarna, J. D. Simon, L. Zecca, F. A. Zucca, A. Napolitano and S. Ito, *Pigment Cell Melanoma Res*, 2015, **28**, 520–544.

5 R. Micillo, L. Panzella, K. Koike, G. Monfrecola, A. Napolitano and M. D'Ischia, *Int J Mol Sci*, , DOI:10.3390/ijms17050746.

6 M. D'Ischia, A. Napolitano, A. Pezzella, P.

Meredith and T. Sarna, *Angewandte Chemie - International Edition*, 2009, **48**, 3914–3921.

7 M. D'Ischia, A. Napolitano, V. Ball, C. T. Chen and M. J. Buehler, *Acc Chem Res*, 2014, **47**, 3541–3550.

8 D. R. Dreyer, D. J. Miller, B. D. Freeman, D. R. Paul and C. W. Bielawski, *Chem Sci*, 2013, **4**, 3796–3802.

9 J. Liebscher, R. Mrówczyński, H. A. Scheidt, C. Filip, N. D. Haìdade, R. Turcu, A. Bende and S. Beck, *Langmuir*, 2013, **29**, 10539–10548.

10 M. Cîrcu and C. Filip, *Polym Chem*, 2018, **9**, 3379–3387.

11 K. S. Schanze, H. Lee and P. B. Messersmith, *ACS Appl Mater Interfaces*, 2018, **10**, 7521–7522.

12 S. H. Yang, S. M. Kang, K. B. Lee, T. D. Chung, H. Lee and I. S. Choi, *J Am Chem Soc*, 2011, **133**, 2795–2797.

13 S. H. Ku, J. S. Lee and C. B. Park, *Langmuir*, 2010, **26**, 15104–15108.

14 G. Wang, H. Huang, G. Zhang, X. Zhang, B. Fang and L. Wang, *Langmuir*, 2011, **27**, 1224–1231.

15 M. H. Ryou, Y. M. Lee, J. K. Park and J. W. Choi, *Advanced Materials*, 2011, **23**, 3066–3070.

16 B. P. Lee, P. B. Messersmith, J. N. Israelachvili and J. H. Waite, *Annu Rev Mater Res*, 2011, **41**, 99–132.

17 Y. Liu, K. Ai and L. Lu, *Chem Rev*, 2014, **114**, 5057–5115.

18 J. H. Ryu, P. B. Messersmith and H. Lee, *ACS Appl Mater Interfaces*, 2018, **10**, 7523–7540.

19 M. E. Lynge, R. Van Der Westen, A. Postma and B. Städler, *Nanoscale*, 2011, **3**, 4916–4928.

20 H. Lee, S. M. Dellatore, W. M. Miller and P. B. Messersmith, *Science (1979)*, 2007, **318**, 426–430.

21 J. H. Waite and M. L. Tanzer, *Science (1979)*, 1981, **212**, 1038–1040.

22 J. H. Waite, *Nat Mater*, 2008, **7**, 8–9.

23 H. Lee, J. Rho and P. B. Messersmith, *Advanced Materials*, 2009, **21**, 431–434.

24 Q. Ye, F. Zhou and W. Liu, *Chem Soc Rev*, 2011, **40**, 4244–4258.

25 N. F. della Vecchia, R. Avolio, M. Alfè, M. E. Errico, A. Napolitano and M. D'Ischia, *Adv Funct Mater*, 2013, **23**, 1331–1340.

26 M. Salomäki, L. Marttila, H. Kivelä, T. Ouvinen and J. Lukkari, *Journal of Physical Chemistry B*, 2018, **122**, 6314–6327.

27 D. R. Dreyer, D. J. Miller, B. D. Freeman, D. R. Paul and C. W. Bielawski, *Chem Sci*, 2013, **4**, 3796–3802.

28 X. Kang, W. Cai, S. Zhang and S. Cui, *Polym Chem*, 2017, **8**, 860–864.

29 R. A. Zangmeister, T. A. Morris and M. J. Tarlov, *Langmuir*, 2013, **29**, 8619–8628.

30 D. R. Dreyer, D. J. Miller, B. D. Freeman, D. R. Paul and C. W. Bielawski, *Langmuir*, 2012, **28**, 6428–6435.

31 N. F. Della Vecchia, A. Luchini, A. Napolitano, G. Derrico, G. Vitiello, N. Szekely, M. Dischia and L. Paduano, *Langmuir*, 2014, **30**, 9811–9818.

32 C. T. Chen, F. J. Martin-Martinez, G. S. Jung and M. J. Buehler, *Chem Sci*, 2017, **8**, 1631–1641.

33 M. L. Alfieri, R. Micillo, L. Panzella, O. Crescenzi, S. L. Oscurato, P. Maddalena, A. Napolitano, V. Ball and M. D'Ischia, *ACS Appl Mater Interfaces*, 2018, **10**, 7670–7680.

34 S. Hong, Y. Wang, S. Y. Park and H. Lee, *Sci Adv*, 2018, **4**, 1–11.

35 Y. Ding, L.-T. Weng, M. Yang, Z. Yang, X. Lu, N. Huang and Y. Leng, *Langmuir*, 2014, **30**, 12258–12269.

36 S. Hong, Y. S. Na, S. Choi, I. T. Song, W. Y. Kim and H. Lee, *Adv Funct Mater*, 2012, **22**, 4711–4717.

37 P. Delparastan, K. G. Malollari, H. Lee and P. B. Messersmith, .

38 J. Liebscher, *European J Org Chem*, 2019, **2019**, 4976–4994.

39 A. P. S. Brogan, L. Bui-Le and J. P. Hallett, *Nat Chem*, 2018, **10**, 859–865.

40 R. P. Swatloski, S. K. Spear, J. D. Holbrey and R. D. Rogers, *J Am Chem Soc*, 2002, **124**, 4974–4975.

41 E. I. Izgorodina, Z. L. Seeger, D. L. A. Scarborough and S. Y. S. Tan, *Chem Rev*, 2017, **117**, 6696–6754.

42 P. Wasserscheid and W. Keim, *Angewandte Chemie - International Edition*, 2000, **39**, 3772–3789.

43 G. Lamoureux, E. Harder, I. v. Vorobyov, B. Roux and A. D. MacKerell, *Chem Phys Lett*, 2006, **418**, 245–249.

44 J. N. Canongia Lopes and A. A. H. Pádua, *Theor Chem Acc*, 2012, **131**, 1–11.

45 L. S. Dodda, I. C. de Vaca, J. Tirado-Rives and W. L. Jorgensen, *Nucleic Acids Res*, 2017, **45**, W331–W336.

46 D. J. Frisch, M. J.; Trucks, G. W.; Schlegel, H. B.; Scuseria, G. E.; Robb, M. A.; Cheeseman, J. R.; Scalmani, G.; Barone, V.; Petersson, G. A.; Nakatsuji, H.; Li, X.; Caricato, M.; Marenich, A. V.; Bloino, J.; Janesko, B. G.; Gomperts, R.; Mennucci, B.; Hratch, 2016.

47 A. J. Stone, *J Chem Theory Comput*, 2005, **1**, 1128–1132.

48 E. Heid, A. Szabadi and C. Schröder, *Physical Chemistry Chemical Physics*, 2018, **20**, 10992–10996.

49 K. Goloviznina, J. N. Canongia Lopes, M. Costa Gomes and A. A. H. Pádua, *J Chem Theory Comput*, 2019, **15**, 5858–5871.

50 A. Dequidt, J. Devémy and A. A. H. Pádua, *J Chem Inf Model*, 2016, **56**, 260–268.

51 A. A. H. Pádua, *Journal of Chemical Physics*, , DOI:10.1063/1.4983687.

52 K. Goloviznina, Z. Gong, M. F. Costa Gomes and A. A. H. Pádua, *J Chem Theory Comput*, , DOI:10.1021/acs.jctc.0c01002.

53 Z. Gong and A. A. H. Padua, *Journal of Chemical Physics*, , DOI:10.1063/5.0040172.

54 P. Eastman, J. Swails, J. D. Chodera, R. T. McGibbon, Y. Zhao, K. A. Beauchamp, L. P. Wang, A. C. Simmonett, M. P. Harrigan, C. D. Stern, R. P. Wiewiora, B. R. Brooks and V. S. Pande, *PLoS Comput Biol*, 2017, **13**, 1–17.

55 C. Y. Son, J. G. McDaniel, Q. Cui and A. Yethiraj, *Journal of Physical Chemistry Letters*, 2019, **10**, 7523–7530.

56 M. Brehm, M. Thomas, S. Gehrke and B. Kirchner, *Journal of Chemical Physics*, , DOI:10.1063/5.0005078.

57 J. A. M. J. Michael W. Schmidt, Kim K. Baldridge, Jerry A. Boatz, Steven T. Elbert, Mark S. Gordon, Jan H. Jensen, Shiro Koseki, Nikita Matsunaga, Kiet A. Nguyen, Shujun Su, Theresa L. Windus, Michel Dupuis, *J Comput Chem*, 1993, **14**, 1347–1363.

58 P. Halat, Z. L. Seeger, S. B. Acevedo and E. I. Izgorodina, *Journal of Physical Chemistry B*, 2017, **121**, 577–588.

59 Z. L. Seeger, R. Kobayashi and E. I. Izgorodina, *Journal of Chemical Physics*, , DOI:10.1063/1.5009791.

60 D. G. Fedorov, *Wiley Interdiscip Rev Comput Mol Sci*, 2017, **7**, 1–17.

61 D. G. Fedorov and K. Kitaura, *The Fragment Molecular Orbital Method: practical applications to large molecular systems*, Taylor & Francis Group, 1st edn., 2009.

62 J. Rigby and E. I. Izgorodina, .

63 S. Y. S. Tan, L. Wylie, I. Begic, D. Tran and E. I. Izgorodina, *Physical Chemistry Chemical Physics*, 2017, **19**, 28936–28942.

64 R. M. Parrish, L. A. Burns, D. G. A. Smith, A. C. Simmonett, A. E. DePrince, E. G. Hohenstein, U. Bozkaya, A. Y. Sokolov, R. di Remigio, R. M. Richard, J. F. Gonthier, A. M. James, H. R. McAlexander, A. Kumar, M. Saitow, X. Wang, B. P. Pritchard, P. Verma, H. F. Schaefer, K. Patkowski, R. A. King, E. F. Valeev, F. A. Evangelista, J. M. Turney, T. D. Crawford and C. D. Sherrill, *J Chem Theory Comput*, 2017, **13**, 3185–3197.

65 S. Tan, S. Barrera Acevedo and E. I. Izgorodina, *Journal of Chemical Physics*, , DOI:10.1063/1.4975326.

66 M. A. Spackman, *J. Comput. Chem.*, 1996, **17**, 1-18.

67 K. Low, S. Y. S. Tan and E. I. Izgorodina, *Front Chem*, 2019, **7**, 208.

68 A. v. Marenich, C. J. Cramer and D. G. Truhlar, *Journal of Physical Chemistry B*, 2009, **113**, 6378–6396.

69 B. Linder, *Thermodynamics and Introductory Statistical Mechanics*, John Wiley & Sons, Ltd, 2005.

70 M. L. Coote, in *Encyclopedia of Polymer Science and Technology*, John Wiley & Sons, Inc., Hoboken, NJ, USA, 2004, pp. 346–347.

71 H. Satria, K. Kuroda, Y. Tsuge, K. Ninomiya and K. Takahashi, *New Journal of Chemistry*, 2018, **42**, 13225–13228.

72 M. C. Foti, L. R. C. Barclay and K. U. Ingold, *J Am Chem Soc*, 2002, **124**, 12881–12888.

73 S. Hesse-Ertelt, T. Heinze, B. Kosan, K. Schwikal and F. Meister, *Macromol Symp*, 2010, **294**, 75–89.

74 S. Y. S. Tan and E. I. Izgorodina, *J Chem Theory Comput*, 2016, **12**, 2553–2568.

75 E. I. Izgorodina and D. R. MacFarlane, *Journal of Physical Chemistry B*, 2011, **115**, 14659–14667.

76 E. I. Izgorodina, D. Golze, R. Maganti, V. Armel, M. Taige, T. J. S. Schubert and D. R. Macfarlane, *Physical Chemistry Chemical Physics*, 2014, **16**, 7209–7221.

77 D. M. Correia, L. C. Fernandes, M. M. Fernandes, B. Hermenegildo, R. M. Meira, C. Ribeiro, S. Ribeiro, J. Reguera and S. Lanceros-Méndez, *Nanomaterials*, , DOI:10.3390/NANO11092401.

78 J. Chen, F. Xie, X. Li and L. Chen, *Green Chemistry*, 2018, **20**, 4169–4200.

79 A. Singh, T. G. Mason, Z. Lu, M. Teo, B. D. Freeman, E. I. Izgorodina, A. Singh, T. G. Mason, Z. Lu, B. M. Teo, E. I. Izgorodina and B. D. Freeman, *Macromol Chem Phys*, 2022, **223**, 2200313.